ACS OMEGA

http://pubs.acs.org/journal/acsodf

Article

Co(II)-Based 2D Coordination Polymer Featuring Energy Storage and Detection of Aqueous Inorganic Anions

Basree,[‖] Arif Ali,[‖] Ganesh Chandra Nayak, Kafeel Ahmad Siddiqui, and Musheer Ahmad*

Cite This: *ACS Omega* 2025, 10, 1344−1353

Read Online

ACCESS | Metrics & More | Article Recommendations | Supporting Information

ABSTRACT: Herein, we have synthesized a Co(II)-based 2D coordination polymer [Co(5-AIA)(Imidazole)]$_n$ (**CP1**) (AIA = 5-aminoisophthalic acid) via a solvothermal approach. SCXRD (single-crystal X-ray diffraction) was utilized to analyze the crystal structure of fabricated **CP1**. Moreover, PXRD, TGA, FTIR, and SEM analyses were done to identify the structural features of fabricated **CP1**. The standard rod depiction of **CP1** exhibits ***hxl*** underlying net topology, and the hydrogen-bonded network depicts ***hcb*** underlying net topology. The fluorescence detection of inorganic anions using **CP1** showed a promising result of 90.3% for MnO_4^-. The electrochemical analysis of **CP1** was done under a basic medium utilizing a 3 M KOH electrolyte through CV (cyclic voltammetry) and GCD (galvanic charge−discharge) techniques which show a 134.75 F g^{-1} specific capacity at a current density of 1 A g^{-1}. Furthermore, **CP1** shows a 94% retention capacity after 2500 cycles at a 20 A g^{-1} current density.

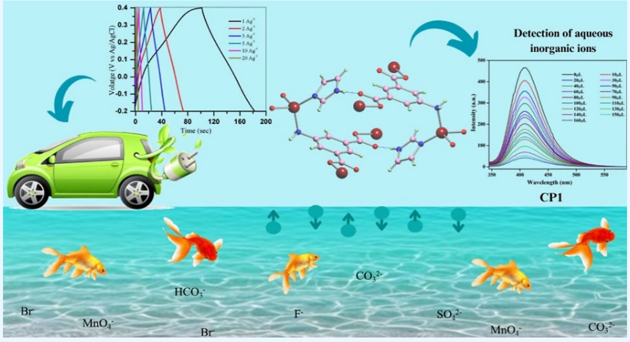

1. INTRODUCTION

In the modern era, environmental pollution has turned into a significant issue for the environment and public health, driven by population growth and industrial development. There are lots of pollutants in air and water pollution such as organic compounds, toxic gases, and heavy metals which are the cause of health risks.[1] MnO_4^- is a strong oxidizing agent. The exploitation and capricious release of MnO_4^- can trigger acute detriment to humans, e.g., coagulative necrosis of the stomach, esophagus, hemorrhage, and liver. Overdosing on MnO_4^- causes allergies, genetic abnormalities, cancer disorders, and carcinogenic effects on cells.[2] Therefore, the US Environmental Protection Agency listed MnO_4^- at the top of the pollutants list.[3] Hence, it is crucial to develop accurate MnO_4^-sensing materials to protect the environment, as well as human health. However, owing to their similar strong oxidizing characteristics, MnO_4^-, CrO_4^{2-}, and $Cr_2O_7^{2-}$ are typically difficult to separate from one another.[4−6] The development of materials with precise selectivity for MnO_4^- sensing is both highly significant and extremely difficult. Hence, it is the need of the hour to develop more efficient and reliable sensing devices. Fluorescence-based CPs are gaining more attention in developing sensing devices owing to their simplicity, operability, selectivity, and sensitivity.[7−10]

Alhaddad and El-Sheikh reported a Co(II)-MOF and examined the detection of various anions. Co(II)-MOF showed better detection of F$^-$ ions with a 0.24 μg/L limit of detection and a 0.72 μg/L limit of quantification.[11] Ma et al. fabricated a new Eu-MOF by utilizing a 4,5-di(3,5-dicarboxylphenoxy)phthalic acid ligand for sensing of MnO_4^- with an 88.2% detection limit.[12]

In recent times, as the population has grown enormously, energy demand has also increased. This growing demand for energy is encouraging scientists to develop new technologies to deliver and store energy in more efficient and sustainable ways as the depletion of fossil fuels, coal, and petroleum is also occurring rapidly.[13] The rapid advancement of electronic devices and vehicles has created an urgent need for novel and better energy storage solutions. Hence, researchers are developing cost-effective, flexible, and high-performance supercapacitor devices to fulfill all of the requirements. SC materials are encouraging choices for energy storage applications.[14−16] The essential functional components of SCs which are responsible for improving power density, better cycling stability, fast charge−discharge rate, and high performance include two electrodes (cathode and anode) where an electrochemical process takes place like charge storage, the electrolyte, which permits ion transport and prevents electronic conduction to complete the electric circuit. Hence, to fulfill all of the properties of SCs, the materials should have enormous

Received: September 29, 2024
Revised: December 2, 2024
Accepted: December 5, 2024
Published: December 24, 2024

ACS Publications

https://doi.org/10.1021/acsomega.4c08913

Scheme 1. Scheme for the Synthesis of CP1

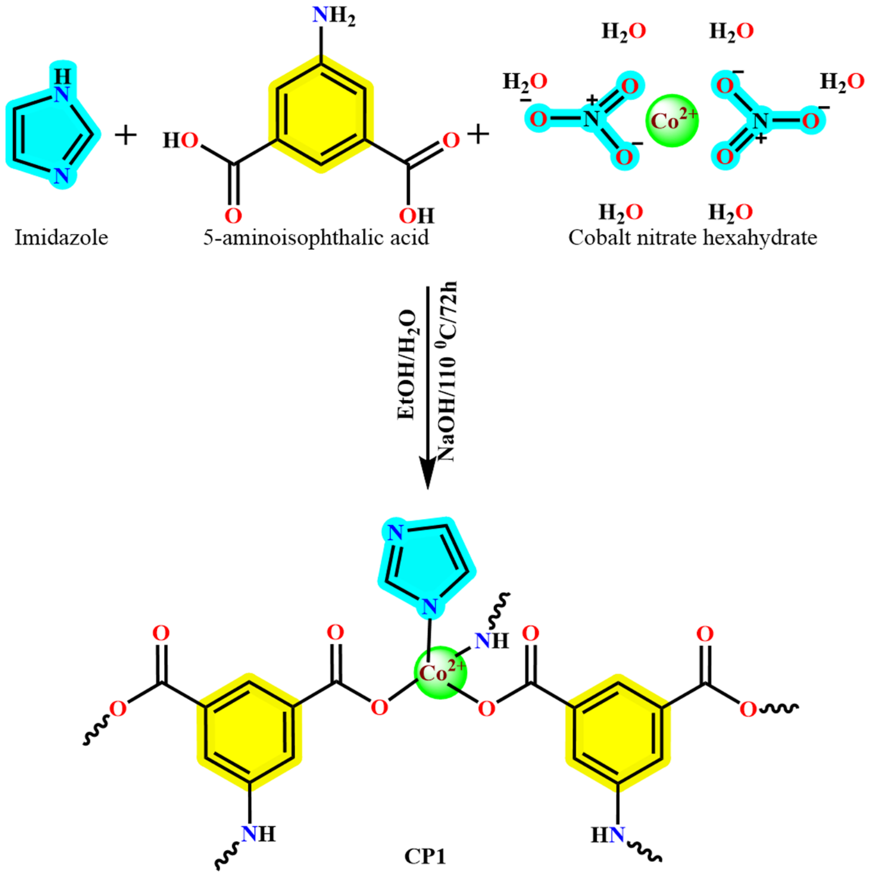

pore size, specific surface area, tunable morphology, good electrical conductivity, and good chemical/mechanical stability. CPs/metal−organic frameworks (MOFs) may meet the criteria for SC materials.

Coordination polymers (CPs) are a family of crystalline materials consisting of metal nodes and organic linkers. CPs show various properties, such as enormous pore size, tunable morphology, specific surface area, chemical/mechanical stability, and good electrical conductivity. CPs show a large number of applications including adsorption,[17−20] catalysis,[21−26] batteries,[27−29] supercapacitors,[30−35] drug delivery,[36−38] sensing,[39−41] magnetism,[42−44] gas storage,[45−47] wastewater treatment,[48,49] separation,[50] and so on.

Somnath et al. reported a 3D Co-MOF named KA@MOF-S utilizing H_3BTC = 1,3,5-benzenetricarboxylic acid and Bimb = 1,4-bis[(1*H*-imidazol-1-yl)methyl]benzene organic ligands under solvothermal conditions. This fabricated MOF facilitates an excellent specific capacity of 648 F g^{-1} at a current density of 1 A g^{-1} with an 89.25% retention stability.[51] Liu et al. developed a two-dimensional nanosheet Co-BTB-LB via a liquid−liquid interface-assisted approach.[52] The developed nanosheet demonstrated an outstanding capacity of 4969.3 F g^{-1} at a current density of 1 A g^{-1}.

A variety of CPs/MOFs (1D−3D) have been investigated in the literature for energy storage and inorganic anion detection. Nitrogen-rich organic ligands provide high basicity for deprotonation and stability to the framework by conjugation and provide versatility in creating functional groups. Moreover, organic ligands having multiple carboxylic groups provide multiple binding sites, higher surface area, fast redox activity, flexibility, etc. Hence, to fulfill our requirement, we have used imidazole and 5-amino isophthalic acid organic ligands to synthesize our material. Herein, we reported the 2D Co(II)-based coordination polymer (**CP1**) for the detection of inorganic anions (F^-, MnO_4^-, Br^-, HCO_3^-, CO_3^{2-}, and SO_4^{2-}). The synthesized **CP1** facilitates outstanding selective detection of MnO_4^- with 90.3%; this result was obtained in triplicate. **CP1** showed good electrochemical energy storage with a specific capacity of 134.7 F g^{-1} at 1 A g^{-1} (current density) with a retention stability of **CP1** of 94% up to 2500 cycles. Hence, CP1 can be used as a potential material for the fabrication of electrodes for energy storage.

2. EXPERIMENTAL SECTION

2.1. Reagents and Materials. Cobalt nitrate hexahydrate [$Co(NO_3)_2 \cdot 6H_2O$], imidazole, and 5-amino isophthalic acid were purchased from Sigma Analytical grade (AR/ACS). All the solvents as well as NaOH were procured from Thermo Fisher Scientific, India, in AR grade. All the chemicals were used without any modification.

2.2. Methods and Instrumentation. The FTIR spectrum of **CP1** was recorded on a Thermo Scientific Nicolet model (iS50) using a KBr disk ranging from 4000 to 400 cm^{-1}. For thermal analysis of **CP1**, a Shimadzu TGA-50H instrument was used. Powder X-ray diffraction patterns were recorded using a Bruker D8 ADVANCE series 2 powder diffractometer (Cu Kα radiation scan rate 30/min, 293 K) in order to analyze the bulk phase purity of **CP1**. The surface morphology as well as mapping and particle heterostructure of **CP1** were analyzed by a scanning electron microscope (JEOL JSM 6510LV

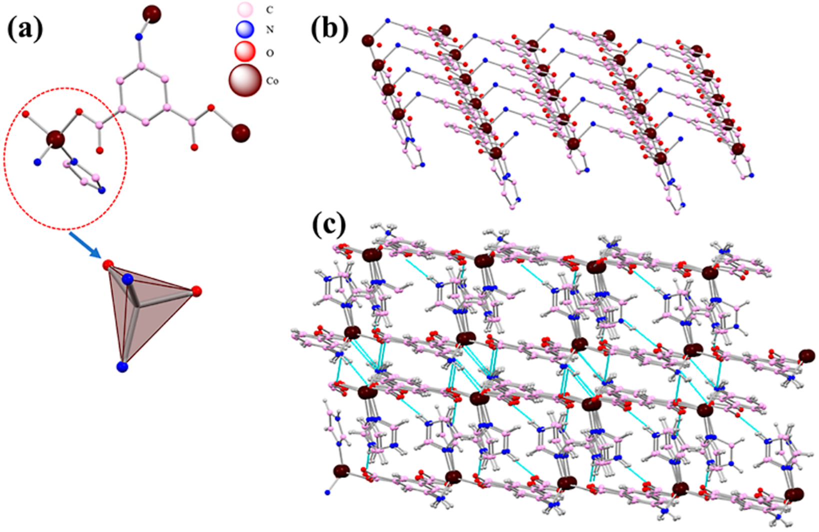

Figure 1. (a) Asymmetric unit of **CP1**, (b) 2D representation of **CP1** along the *b*-axis, (c) 3D view of **CP1** via hydrogen bonding.

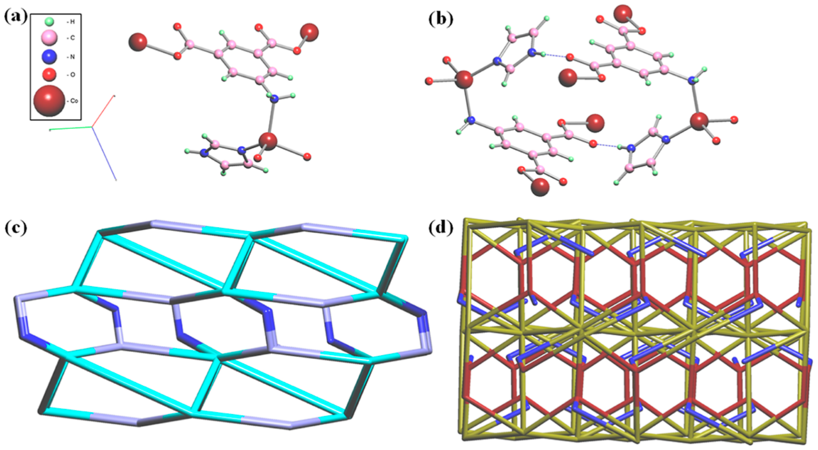

Figure 2. (a) Molecular representation of **CP1**, (b) hydrogen-bonded 3D structure of **CP1**, (c) ***hxl*** underlying net representation, and (d) hydrogen-bonded topological view of **CP1** along the *b*-axis, with ***hcb*** underlying net topology.

model) instrument coupled with JEOL/EO formate. The electrochemical analysis of **CP1** was carried out on an electrochemical workstation (Metrohm Autolab M204) at room temperature with a three-electrode system.

2.3. Single-Crystal X-ray Refinement.

The crystallographic data of **CP1** was acquired by employing "XtaLAB Synergy, Rigaku, Japan" at a temperature of 293(2) K. The radiation utilized was monochromatic Mo Kα radiation with a wavelength of 0.71073 Å. The determination of the crystal structure was done by utilizing Olex2,[53] which was further solved with the olex-2.solve[54] structure solution program by employing charge flipping. Subsequently, Gauss−Newton minimization technology was implemented to improve the structure using the olex2.refine[54] refinement software. Table S1 summarizes the data pertaining to the crystal structure refinement of **CP1**, as well as other evidence related to the bond lengths and bond angles of **CP1** (Tables S2 and S3).

2.4. Synthesis of CP1.

The synthesis of **CP1** has been done via a solvothermal approach. A mixture of 10 mg of imidazole (0.15 mmol) was taken in a beaker and dissolved in distilled water with continuous stirring for 30 min, and 20 mg of 5-aminoisophthalic (0.11 mmol) acid was taken in a separate beaker and dissolved in ethanol with continuous stirring for 30 min. 80 mg of cobalt nitrate was added to the aqueous solution of imidazole with a few drops of NaOH to make the solution slightly alkaline. After 30 min, an ethanolic solution of 5-aminoisophthalic acid was poured into an aqueous solution of imidazole and the mixture was stirred for 10 min again. After stirring, the mixture was poured into a stainless-steel Teflon autoclave and put into a hydrothermal oven at 110 °C for 72 h. After 72 h, the mixture was cooled down at its own temperature for the next 12 h and then the mixture was filtered. Upon filtration, we got purple crystals which were appropriate for SCXRD (Scheme 1). Yield: 82%, IR (cm^{-1}): 3445 (br), 3256 (d), 3073 (s), 2958 (m), 2397 (m), 1772 (s), 1623 (s), 1548 (s), 1364 (d), 1083 (m), 808 (m), 722 (m), 648 (m), 590 (m), 447 (m).

2.5. Fabrication of Electrodes.

The electrochemical study of **CP1** was achieved by a three-electrode system in 3 M KOH. The reference electrode was fabricated with Ag/AgCl, and the counter electrode was fabricated with platinum. The working electrode was fabricated with **CP1** (80%), poly(vinylidene fluoride) (PVDF) (10%), and carbon black (10%). The prepared electrode material was coated on a circular graphitic rod. Thorough electrochemical analysis was performed using various techniques like CV (cyclic voltam-

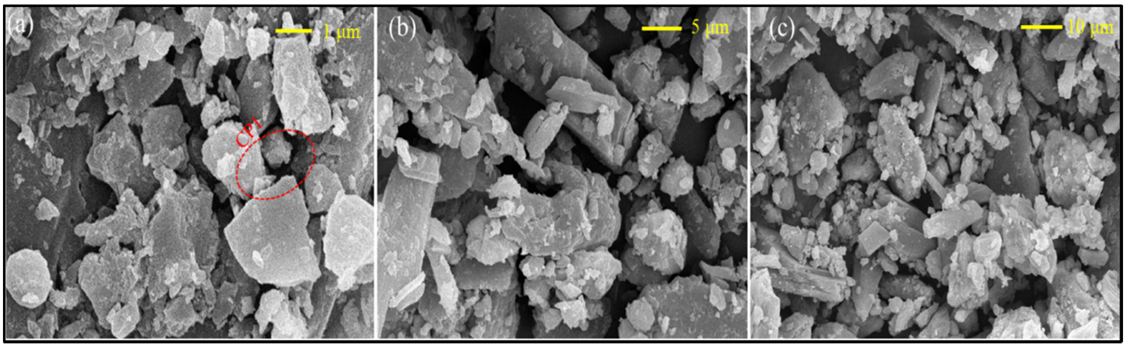

Figure 3. SEM images of **CP1** at various magnification ranges (a−c).

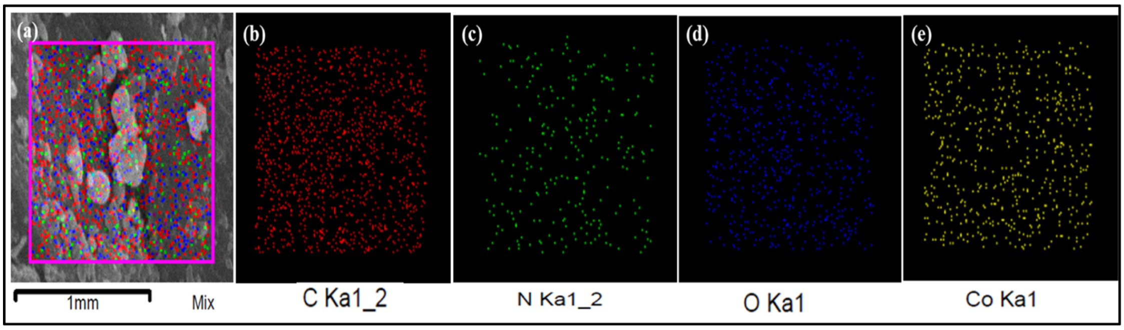

Figure 4. Elemental mapping of **CP1** was recorded at a 1 mm mixed selective area (a−e).

metry), GCD (galvanostatic charge−discharge), and EIS (electrochemical impedance spectroscopy) using Metrohm Autolab.

2.6. Efficiency Performance Evaluation. The specific capacitance (in F g^{-1}) of **CP1** was evaluated by using the equation given below

$$C_p = \frac{I \times \Delta t}{m \times \Delta v} \tag{1}$$

in which I denotes constant current, m denotes the mass of the electroactive material (i.e., I/m = current density), and Δt and Δv signify constant discharge duration and potential window, respectively.

3. RESULTS AND DISCUSSION

3.1. Structural Description and Topological Analysis of CP1. Single-crystal X-ray diffraction was utilized for the crystal analysis, and it showed that the crystal crystallizes in a monoclinic system with the $P2_1/c$ space group. The asymmetric unit of **CP1** governs a single unit of Co(II) ion, 5-amino isophthalic acid, and imidazole linker (Figure 1a) that shows distorted tetrahedral geometry. The extended 2D network of **CP1** shows a stair pattern (Figure 1b). Further, the hydrogen-bonding interaction constructs a 3D supramolecular network (Figure 1c). Topological analysis of **CP1** was examined by utilizing Topos Pro software (Figure 2a,b).[55,56] The standard rod net depiction of **CP1** shows PS: $\{3^6{\cdot}4^6{\cdot}5^3\}$, uninodal net that governs ***hxl*** underlying net (Figure 2c). Further, simplifying the TTD collection of hydrogen-bonded network of **CP1** shows a point symbol for the net: $\{4^3{\cdot}6^2{\cdot}8\}\{4^9{\cdot}6^8{\cdot}8^4\}\{6\}$ with (2-c)(4-c)(7-c); 3-nodal net with ***hcb*** underlying net topology (Figure 2d).

3.2. PXRD, FTIR, TGA, and SEM Analysis. A single-crystal X-ray diffraction technique was employed to establish the crystal structure of **CP1**. Other chemical and physical analyses, for instance, bulk phase purity, thermal stability, surface morphology, and functionality, were done by PXRD, TGA, SEM, and FTIR techniques, respectively. The bulk phase purity analysis was performed by powder X-ray diffraction technique which reveals that the PXRD pattern is in good agreement with the simulated pattern of **CP1** (Figure S1). Powder X-ray diffraction of **CP1** is also performed after the electrochemical study which reveals that PXRD patterns are perfectly matched before and after the electrochemical study of **CP1** (Figure S1). TGA was performed under a N_2 atmosphere at the rate of 10 °C/min to examine the thermal stability. In the TGA plot of **CP1**, three stages of weight loss are examined in the temperature interval between 103 and 485 °C. The first stage from 103 to 203 °C is due to the water loss. Moreover, 18% weight loss was observed at 225 °C which is attributed to the elimination of the organic ligand (imidazole). The thermal stability plateau at 225−410 °C is followed by a further weight loss phase where the primary framework collapses. At 400 °C, the disintegration process is complete, and weight loss is gradual (Figure S2). The FTIR study reveals the vibrational bands at various frequencies due to the presence of Co−N, Co−O, C═N, C−H, C−N, C═O, and C═C bonds.[57,58] The FTIR spectrum exhibits a wide peak at 3445 cm^{-1} corresponding to the −OH functional group. The vibrational peak at 3256 cm^{-1} could be due to the presence of the −NH functional group. The vibrational frequencies at 3073 and 2958 cm^{-1} could be due to the presence of −CH bonds of the benzene ring of the complex. The vibrational frequencies at 722 and 648 cm^{-1} correspond to the presence of Co−O bonds, and the other vibrational bands at 590 and 447 cm^{-1} correspond to the presence of Co−N bonds (Figure S3). To determine the surface morphology of **CP1**, SEM analysis was performed at various magnification ranges (Figure 3). The SEM images of **CP1** revealed that **CP1** contains a granular

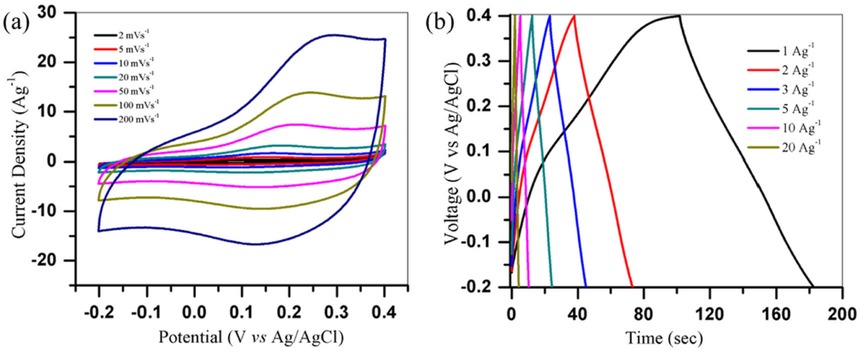

Figure 5. (a) CV profile of **CP1** at various scan rates and (b) GCD of **CP1** at various scan rates.

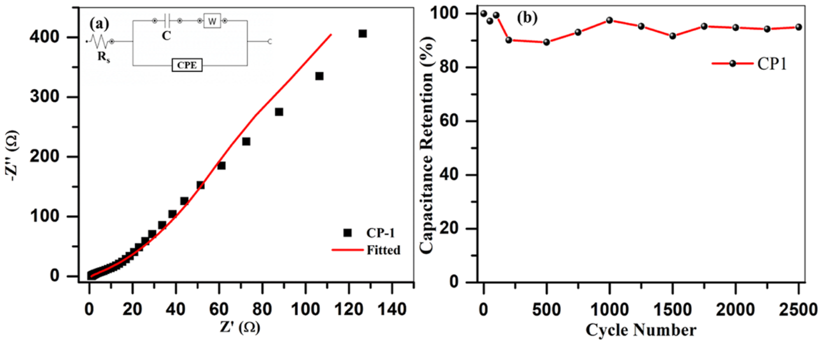

Figure 6. (a) Nyquist plot for the **CP1** electrode material (inset figure for fitted circuit) and (b) cyclic stability of **CP1** at a current density of 20 A g^{-1}.

morphology at various magnification ranges. The granular morphology could be ascribed to offering a larger surface area that enhances more reactive sites for the electrochemical process and also reduces the diffusion length to boost the reaction rate. Moreover, the elemental composition of **CP1** was estimated by elemental mapping at the 1 mm range of specific elements (Figure 4).

3.3. Electrochemical Studies. Coordination polymers (CPs) are competitive materials for energy storage applications as they have tunable structural topology, prominent pore size, and large surface area. CPs containing metals like Co, Ni, and Cu have been shown to outshine the pseudocapacitive nature for energy storage applications. The electrochemical analysis of the fabricated electrode with **CP1** was performed using CV at several scan rates (2−200 mV s^{-1}) within the potential window (−0.2 to 0.4 V) in 3 M KOH. Cyclic voltammetry discloses various features of working electrodes. **CP1** showed differentiable peaks at 0.16 and 0.07 V corresponding to the redox couple of Co(II)/Co(III), which show its electrochemical activity. Again, the alignment of the CV spectrum of **CP1** with the EDLC (electric double-layer capacitance) mechanism shows semirectangular features which reveal effective charge propagation on the surface of the electrode material.

Figure 5a shows the CV plots of the active electrode material across several scan rates varying between 2 and 200 mV s^{-1}. Additionally, the area inside every CV curve grows as scan rates rise for both redox peaks. Particularly, the integrated surface area of the **CP1** electrode surpasses, resulting in a significant increase in specific capacitance. But at greater scan rates, the electrode tends to take on a semirectangular shape, indicating that electrolyte ions diffuse faster. This process probably helps to boost the energy storage efficiency, as seen in Figure 5a. The **CP1** structure facilitates more effective charge transfer by expanding the system's area of contact and modes.

GCD analysis was accomplished within a potential window of −0.2 to 0.4 V at several current densities from 1 to 20 A g^{-1} for the evaluation of the capacitive behavior of the fabricated electrode **CP1** in a 3 M KOH aqueous electrolyte solution, as shown in Figure 5b. The discharging time decreases as the current density increases, and capacitance also decreases. When the current density is 1 A g^{-1}, **CP1** demonstrates a 134.75 F g^{-1} specific capacitance. The GCD curves are not perfectly triangular shapes with nonlinear characteristics which indicates that **CP1** shows pseudocapacitive behavior. Furthermore, as the current density increases from 1, 2, 3, 5, 10, to 20 A g^{-1}, the specific capacitance drops from 134.75, 117.3, 109.5, 100, 85.8, to 71.6 F g^{-1}, respectively. The redox characteristics at the electrode/electrolyte interface may be caused by the decrease in specific capacitance with an increase in the current density. This exceptional specific rate performance of **CP1** could be ascribed to its porous features and electron hoping due to 5-amino isophthalic acid as well as imidazole linkers. Hence, based on the aforementioned results, **CP1** could be a good electrode material for energy storage.

Moreover, in Figure 6, the EIS spectrum is plotted for the quantitative evaluation of SC electrodes over the 100 kHz−0.01 Hz frequency range at a 10 mV potential amplitude. The EIS spectrum reveals that the **CP1** electrode can feature lower series resistance (R_s, encompassing solution resistance, contact resistance, etc.) and charge-transfer resistance (R_{ct}). Electrical resistance may be due to the rapid flow of electrons and electrolytic ions. The Nyquist plot for the **CP1** electrode exhibits a pattern consisting of a slight semicircle that is attributed to the high-frequency region and a straight line in the low-frequency region, depicting solution resistance and

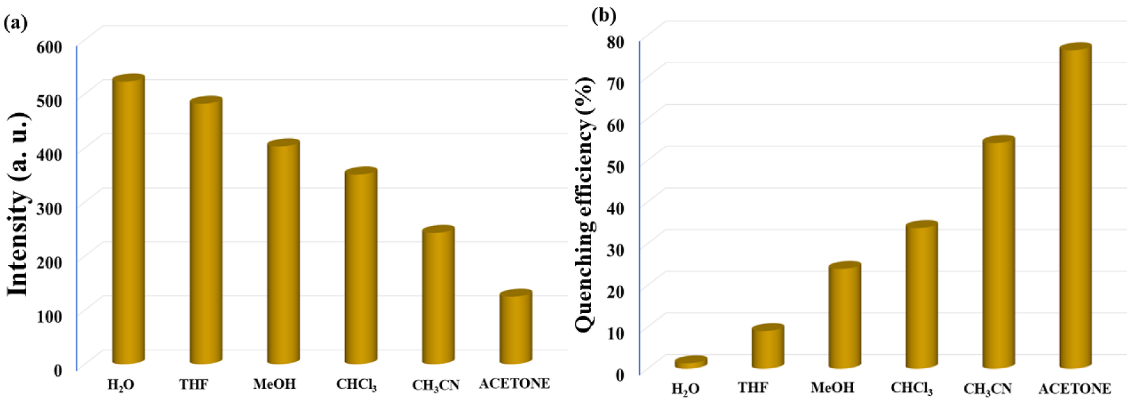

Figure 7. (a) Levels of fluorescence intensity for **CP1** at different solvent concentrations and (b) relative efficiencies of fluorescence quenching for **CP1** in water-based solutions with different solvent concentrations.

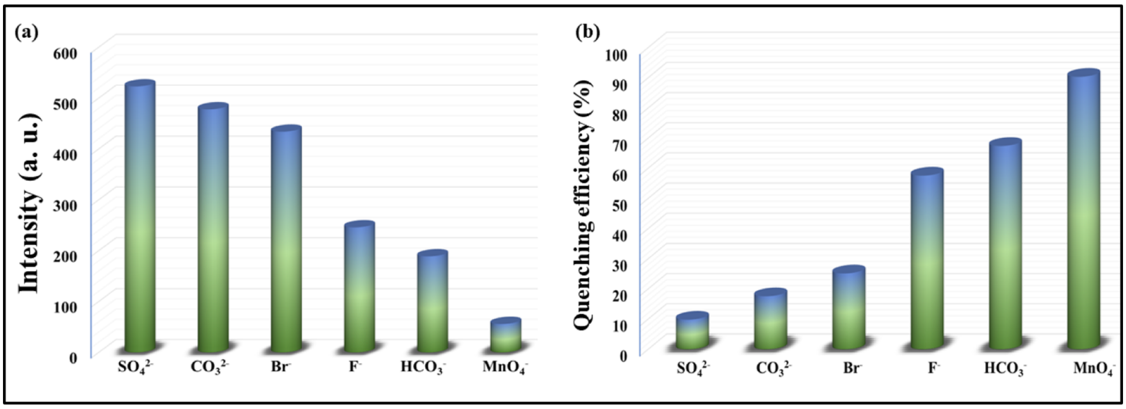

Figure 8. (a) The amount of fluorescence intensity and (b) the relative fluorescence quenching rates of **CP1** in water solutions (5×10^{-4} M) of different inorganic anions.

linear diffusion, respectively, as depicted in Figure 6a. EIS data were fitted to an equivalent circuit; the R_s value calculated from the points where the curves intersect the Z' axis (real axis) was 952 mΩ, signifying minimum resistance in the **CP1** electrode material. Furthermore, the simulated C (pseudo-capacitance) and CPE (double layer) values were obtained to be 49.6 mF and 2.19 $\text{m}\Omega^{-1}\cdot\text{s}^{N}$ (N = 0.998), respectively, attributed to charge storage via the redox reaction and electrode/electrolyte junction interface.[59,60] In the higher-frequency region, a slight semicircle appeared for Warburg (27.0 $\text{m}\Omega^{-1}\cdot\text{s}^{1/2}$) that denoted linear diffusion. These findings demonstrate that the best conditions for creating the **CP1** electrode material are a lower concentration and a longer soaking time.

Furthermore, the long-term stability of the electrode material (**CP1**) was examined using charging−discharging at a 20 A g^{-1} current density with the same potential window of CV and GCD that shows ∼94% retention capacity after completing 2500 cycles, as shown in Figure 6b. The specific capacitance also increased as compared to the obtained GCD at 20 A g^{-1}, and this phenomenon could have occurred due to pore expansion after electrolyte insertion/desertion or rapid electrolyte ion transport into the electrode material. We have compared several reported Co(II) based CPs, showing that **CP1** is suitable for an electrode material (Table S4).

3.4. Luminescence Sensing.

In order to obtain a more thorough understanding of the sensing capacities of the produced **CP1**, we investigated sensing experiments in several solvents. To perform fluorescence sensing, a 3 mg sample of crystalline **CP1** was immersed in 4 mL of different solvents, including water (H_2O), tetrahydrofuran (THF), methanol (MeOH), chloroform ($CHCl_3$), acetonitrile (CH_3CN), and acetone. For 30 min, the solution was subsequently exposed to ultrasonic treatment and kept for 24 h to create stable suspensions. The fluorescence emission of the suspensions was monitored across the 200−600 nm range at ambient temperature after being excited at 300 nanometers. The fluorescence intensity levels of stable solutions of **CP1** varied according to the solvent used (Figure 7a). The water solution of **CP1** exhibited a remarkable emission intensity of 545 nm upon excitation at 300 nm (Figure 7b). To get the efficiency of luminescence emission (Q), eq 2 was utilized. Fluorescence quenching was also examined through the application of Stern−Volmer (S−V) eq 3.

$$Q\ (\%) = \{(I_0 - I)/I_0\} \times 100 \tag{2}$$

$$I_0/I = 1 + K_{SV}[M] \tag{3}$$

where K_{SV} implies the quenching constant and $[M]$ signifies the molar concentration of the material. I_0 and I represent fluorescence emission intensities, respectively, before and after the introduction of the samples.[61]

3.5. Detection of Anions.

To find out how well **CP1** can find inorganic anions, water solutions were mixed with 5×10^{-4} M of various K_nX ($X = MnO_4^-$, Br^-, CO_3^{2-}) and Na_nX ($X = F^-$, HCO_3^-, SO_4^{2-}) anions. Figure 8a shows the relative levels of **CP1** fluorescence intensities in water solutions (5×10^{-4} M) of different inorganic anions. It was found that the

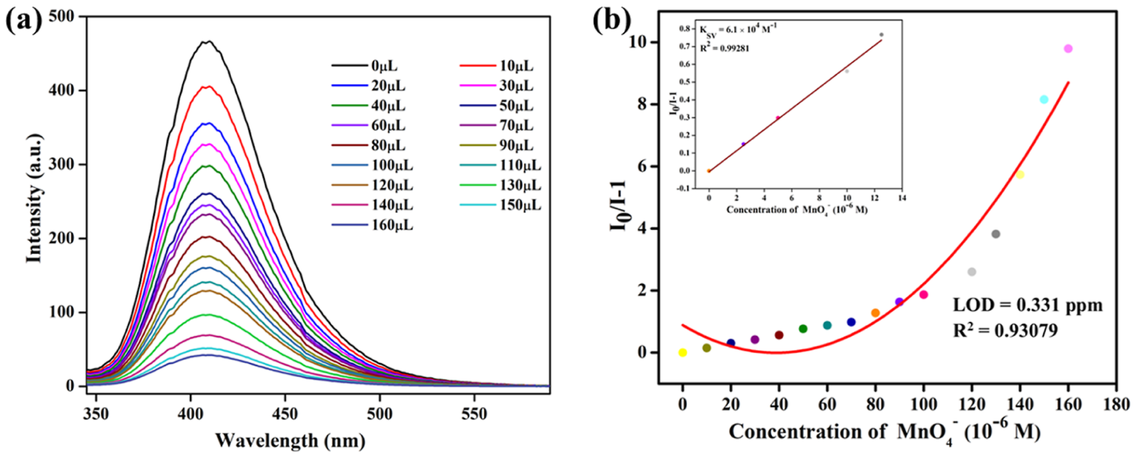

Figure 9. (a) Illustrates the observed intensity of fluorescence emission as specific compounds are incrementally added to the aqueous solutions of **CP1**. The panel displays the outcomes upon the addition of MnO_4^-, and (b) shows the S−V plot of **CP1** distributed in water following a progressive injection of MnO_4^- at a concentration of 1 mM. The graph shows the linear relationship between the concentration of MnO_4^- and the S−V curve of **CP1** at low concentrations (inset).

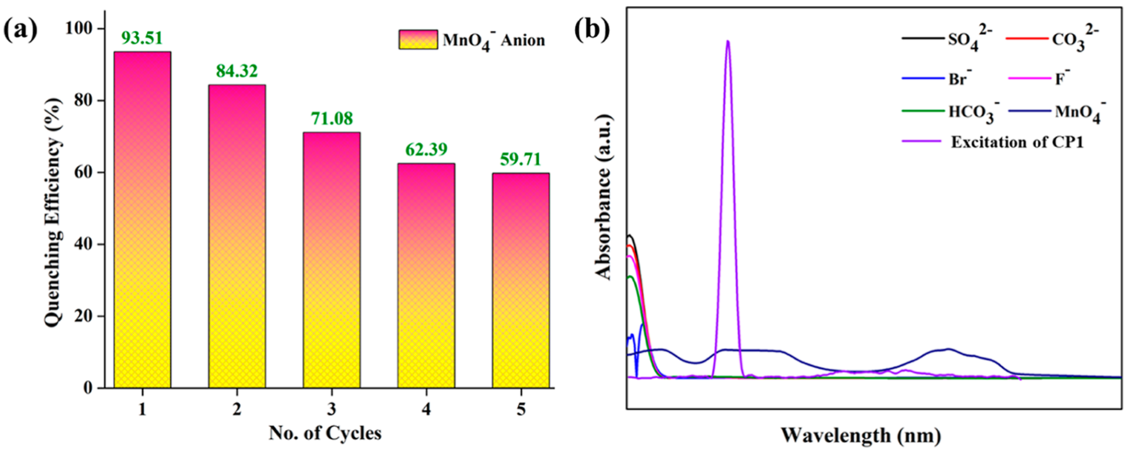

Figure 10. (a) Recyclability and reusability of **CP1** for each cycle for MnO_4^- and (b) spectral overlap between the UV−vis absorption spectra of anions with the excitation spectra of **CP1**.

quenching efficiencies are 57.5% (F^-), 90.3% (MnO_4^-), 25.7% (Br^-), 67.4% (HCO_3^-), 17.5% (CO_3^{2-}), and 9.8% (SO_4^{2-}) (Figure 8b). It is interesting that MnO_4^- (90.3%) causes the highest quenching efficiency compared with other anions. This shows that MnO_4^- is very selective for being detected out of all of the anions that were tested. We tested how sensitive MnO_4^- is as a sensor in water by performing a quantitative fluorescence titration experiment. A water-based solution (1 mM) of MnO_4^- was added drop by drop to a stable **CP1** solution that was spread out. After the solution became stable, the fluorescence intensity was determined separately. Gradually increasing the concentration of anions decreased the fluorescence intensity (Figure 9a). The Stern−Volmer (S−V) equation was also used to find the value of K_{SV}: $I_0/I = 1 + K_{SV}[M]$. The experimental data show that there is a linear association between the amount of MnO_4^- ($R^2 = 0.99281$) and the calculated value of K_{SV} at a low concentration of 6.1×10^4 M^{-1} for MnO_4^-. The quench plot in Figure 9b shows that at low amounts, the rate of quenching is related in a straight line. Calculating LOD = $3\sigma/m$ (where m signifies the slope and σ is used for the standard error) gives us the minimum detection limit for MnO_4^-, which is 2.1×10^{-6} M (0.331 ppm). This means that **CP1** can be utilized as a very sensitive fluorescence sensing material to measure the amount of the MnO_4^- anion present.

3.6. Recyclability and Reusability. The purpose of observing the fluorescence emission spectra of **CP1** in an aqueous solution was to determine its effectiveness as a fluorescence sensor for the MnO_4^- anions. It is possible to reuse the fluorescence intensity of **CP1** for a minimum of five cycles, as shown in Figure 10a.

3.7. Possible Mechanism of Fluorescence Quenching. Recent research has suggested that framework collapse, ion exchange between different analytes, and competitive absorption/interaction mechanisms are frequently implicated in the identification of inorganic anions and solvents.[62] To get a better understanding of how **CP1** senses MnO_4^- through quenching impacts, supplementary analyses were executed. The UV−vis spectra were used to recognize the inhibition mechanism caused by MnO_4^-. The breakdown of **CP1** is unreliable for fluorescence quenching.[63,64] The energy transfer reduction between the π & π^* orbitals of the N-containing ligands is responsible for the drop in fluorescence intensity seen amid the electron-transfer transitions of MnO_4^-. To capture the sensing information, we used an excitation wavelength of 300 nm. This particular wavelength was selected to ensure maximal absorption and effective excitation since it matches the excitation peak fluorophore. We obtained the best fluorescence emission at 300 nm, which improved the sensitivity and accuracy of the experiment. Additionally, by reducing the background influence, this decision produces more accurate and consistent findings for the experimental setup. The probability of resonance energy transfer is established by the extent of spectral overlap between the excitation bands of the fluorescence detectors **CP1** and the absorption bands of the inorganic anions (analytes). The mechanism aligned with the ones reported by other teams. MnO_4^- is more likely to quench than other inorganic anions because of its UV−vis absorption spectra that overlap with the excitation spectra of **CP1** (Figure 10b). From these variables, it can be concluded that inorganic anions compete with organic ligands for the absorption of excitation wavelength energy, as indicated by the overlaps between **CP1** and MnO_4^- UV−vis spectra. Quenching occurs as a result of this competition.[65,66]

4. CONCLUSIONS

In summary, the fabrication of a new 2D coordination polymer, $[Co(5\text{-}AIA)(imidazole)]_n$ (**CP1**), was done through the solvothermal method. **CP1** exhibited a ***hcb*** underlying net topology. **CP1** exhibits outstanding specific fluorescence detection characteristics for inorganic anions (MnO_4^-). Furthermore, **CP1** facilitates better electrochemical energy storage capacity in the 3 M KOH electrolyte. However, **CP1** exhibits remarkable stability with a low R_{ct} value and enormous specific capacitance. So, **CP1** can be potentially employed in inorganic anion detection and electrochemical energy storage.

■ ASSOCIATED CONTENT

Data Availability Statement

No data was used for the research described in the article.

Supporting Information

The Supporting Information is available free of charge at https://pubs.acs.org/doi/10.1021/acsomega.4c08913. This data can be obtained free of charge via http://www.ccdc.cam.ac.uk/conts/retrieving.html, or from the Cambridge Crystallographic Data Centre, 12 Union Road, Cambridge CB2 1EZ, UK; Fax: (+44) 1223-336-033; or Email: deposit@ccdc.cam.ac.uk.

Single-crystal data of **CP1** (CIF)

Crystal data and structure refinement, bond lengths, and bond angles for **CP1**; PXRD patterns of simulated **CP1**, as-synthesized **CP1**, and after electrochemistry of **CP1**; thermogravimetric curve of as-synthesized CP (**CP1**); FTIR spectrum of **CP1**; and comparative study of various reported Co(II)-based CPs (PDF)

■ AUTHOR INFORMATION

Corresponding Author

Musheer Ahmad − *Department of Applied Chemistry, ZHCET, Faculty of Engineering and Technology, Aligarh Muslim University, Aligarh, Uttar Pradesh 202002, India;* orcid.org/0000-0002-7446-0232; Email: amusheer4@gmail.com

Authors

Basree − *Department of Applied Chemistry, ZHCET, Faculty of Engineering and Technology, Aligarh Muslim University, Aligarh, Uttar Pradesh 202002, India*

Arif Ali − *Department of Chemistry & Chemical Biology, Indian Institute of Technology (ISM), Dhanbad 826004 Jharkhand, India;* orcid.org/0000-0002-8776-8201

Ganesh Chandra Nayak − *Department of Chemistry & Chemical Biology, Indian Institute of Technology (ISM), Dhanbad 826004 Jharkhand, India;* orcid.org/0000-0003-4470-9268

Kafeel Ahmad Siddiqui − *Department of Chemistry, National Institute of Technology Raipur, Raipur, Chhattisgarh 492010, India*

Complete contact information is available at: https://pubs.acs.org/10.1021/acsomega.4c08913

Author Contributions

‖Basree and A.A. contributed equally to the article. **Basree**: writing—original draft, data curation, conceptualization, methodology, review and editing, formal analysis; **A. Ali**: Writing—original draft, data curation, conceptualization, methodology, review and editing; **G. C. Nayak**: formal analysis; **K. A. Siddiqui**: visualization, writing—review and editing; **M. Ahmad**: supervision, conceptualization, methodology, software, formal analysis, writing—review and editing.

Notes

The authors declare no competing financial interest.

■ ACKNOWLEDGMENTS

The authors thank the Department of Applied Chemistry, Faculty of Engineering and Technology, Aligarh Muslim University, U.P., India, for providing research laboratory facilities. Basree thanks the DST/INSPIRE Fellowship/2021/IF210635. A.A. also thanks to the Institute Post-Doctoral fellowship (DAR/IPDF/CCB/53/2023), Indian Institute of Technology (ISM), Dhanbad. M.A. acknowledges the Start-up grants from the UGC, India.

■ REFERENCES

(1) Lustig, W. P.; Mukherjee, S.; Rudd, N. D.; Desai, A. V.; Li, J.; Ghosh, S. K. Metal−Organic Frameworks: Functional Luminescent and Photonic Materials for Sensing Applications. *Chem. Soc. Rev.* **2017**, *46* (11), 3242−3285.

(2) Lin, Z.; Li, W.; Chen, Q.; Chen, L.; Zhang, C.; Zhang, J. A New Photochromic-Ligand-Based Luminescent Coordination Polymer as a MnO_4^- Sensor with Extremely High Sensitivity and Excellent Selectivity. *J. Mater. Chem. C* **2022**, *10* (5), 1672−1680.

(3) Oliver, S. R. J. Cationic Inorganic Materials for Anionic Pollutant Trapping and Catalysis. *Chem. Soc. Rev.* **2009**, *38* (7), 1868.

(4) Wang, Y. N.; Wang, S. D.; Chang, X. P.; Li, H. F.; Zhang, J. M.; Xu, L.; Wang, S. Y. A New Fluorescence MOF for Highly Sensitive Detection of Acetylacetone. *ChemistrySelect* **2021**, *6* (5), 968−973.

(5) Zhang, J.; Yue, Y.; Tao, X.; Zhang, J.; Yin, D.; Zhang, C. A Photochromic Metal−Organic Framework with a Rare 3D Self-Interpenetrated Architecture and an Ultrahigh MnO_4^- Sensing Ability. *New J. Chem.* **2024**, *48* (28), 12609−12615.

(6) Sang, X.; Liu, D.; Song, J.; Wang, C.; Nie, X.; Shi, G.; Xia, X.; Ni, C.; Wang, D. High-Efficient Liquid Exfoliation of 2D Metal-Organic Framework Using Deep-Eutectic Solvents. *Ultrason. Sonochem.* **2021**, *72*, 105461.

(7) Fang, X.; Zong, B.; Mao, S. Metal−Organic Framework-Based Sensors for Environmental Contaminant Sensing. *Nano-Micro Lett.* **2018**, *10* (4), 64.

(8) Zhao, Y.-Y.; Chen, L.; Xu, Z.; Zhu, C.-Y.; Li, P.; Gao, W.; Li, J.-Y.; Zhang, X.-M. Microporous Cd-MOF as Multifunctional Material for Rapid and Visual Luminescence Sensing of Fe3+, MnO4− and TNP in Water and Efficient CO2 Catalytic Conversion. *Microporous Mesoporous Mater.* **2023**, *362*, 112764.

(9) Yuan, R.; Huang, K.; Zou, Y.; Zhang, X.; Qin, D. Two Multifunctional Luminescent Cobalt Metal-Organic Frameworks for Selectively and Sensitively Sensing of Cu2+, MnO4- and Picric Acid in Water. *J. Solid State Chem.* **2022**, *307*, 122875.

(10) Chen, W.; Lin, H.; Wu, Y.; Yang, M.; Zhang, X.; Zhu, S.; He, M.; Xie, J.; Shi, Z. Fluorescent Probe of Nitrogen-Doped Carbon Dots Derived from Biomass for the Sensing of MnO4− in Polluted Water Based on Inner Filter Effect. *Adv. Compos. Hybrid Mater.* **2022**, *5* (3), 2378−2386.

(11) Alhaddad, M.; El-Sheikh, S. M. Selective and Fast Detection of Fluoride-Contaminated Water Based on a Novel Salen-Co-MOF Chemosensor. *ACS Omega* **2021**, *6* (23), 15182−15191.

(12) Ma, Y.; Zhu, M.; Zhang, Y.; Sun, Y.; Wu, S. A Water-Stable Eu-MOF as Multi-Responsive Luminescent Sensor for High-Efficiency Detection of Fe3+, MnO4− Ions and Nicosulfuron in Aqueous Solution. *J. Solid State Chem.* **2022**, *316*, 123598.

(13) Liang, H.; Liu, Y.; Zuo, F.; Zhang, C.; Yang, L.; Zhao, L.; Li, Y.; Xu, Y.; Wang, T.; Hua, X.; Zhu, Y.; Li, H. $Fe_2(MoO_4)_3$ Assembled by Cross-Stacking of Porous Nanosheets Enables a High-Performance Aluminum-Ion Battery. *Chem. Sci.* **2022**, *13* (47), 14191−14197.

(14) Nixon, E. J.; Jayapaul, A.; Chung, R.-J.; Rajkumar, S.; Merlin, J. P. Antimony Vanadate Spheres: Synthesis, Characterizations, and Use as Positive Electrode in Asymmetric Supercapacitor Systems. *J. Electroanal. Chem.* **2024**, *953*, 118014.

(15) Cao, X.; Tan, C.; Sindoro, M.; Zhang, H. Hybrid Micro-/Nano-Structures Derived from Metal−Organic Frameworks: Preparation and Applications in Energy Storage and Conversion. *Chem. Soc. Rev.* **2017**, *46* (10), 2660−2677.

(16) Ma, Y.; Zhang, L.; Yan, Z.; Cheng, B.; Yu, J.; Liu, T. Sandwich-Shell Structured $CoMn_2O_4$/C Hollow Nanospheres for Performance-Enhanced Sodium-Ion Hybrid Supercapacitor. *Adv. Energy Mater.* **2022**, *12* (11), 2103820.

(17) Maia, R. A.; Louis, B.; Gao, W.; Wang, Q. CO_2 Adsorption Mechanisms on MOFs: A Case Study of Open Metal Sites, Ultra-Microporosity and Flexible Framework. *React. Chem. Eng.* **2021**, *6* (7), 1118−1133.

(18) Barpaga, D.; Nguyen, V. T.; Medasani, B. K.; Chatterjee, S.; McGrail, B. P.; Motkuri, R. K.; Dang, L. X. Insight into Fluorocarbon Adsorption in Metal-Organic Frameworks via Experiments and Molecular Simulations. *Sci. Rep.* **2019**, *9* (1), 10289.

(19) Zhang, B.; Zhu, Z.; Wang, X.; Liu, X.; Kapteijn, F. Water Adsorption in MOFs: Structures and Applications. *Adv. Funct. Mater.* **2024**, *34*, 2304788.

(20) Muslim, M.; Ali, A.; Kamaal, S.; Ahmad, M.; Jane Alam, M.; Rahman, Q. I.; Shahid, M. Efficient Adsorption and Facile Photocatalytic Degradation of Organic Dyes over H-Bonded Proton-Transfer Complex: An Experimental and Theoretical Approach. *J. Mol. Liq.* **2022**, *347*, 117951.

(21) Goswami, A.; Ghosh, D.; Chernyshev, V. V.; Dey, A.; Pradhan, D.; Biradha, K. 2D MOFs with Ni(II), Cu(II), and Co(II) as Efficient Oxygen Evolution Electrocatalysts: Rationalization of Catalytic Performance *vs* Structure of the MOFs and Potential of the Redox Couples. *ACS Appl. Mater. Interfaces* **2020**, *12* (30), 33679−33689.

(22) Gopi, S.; Al-Mohaimeed, A. M.; Al-onazi, W. A.; Soliman Elshikh, M.; Yun, K. Metal Organic Framework-Derived Ni-Cu Bimetallic Electrocatalyst for Efficient Oxygen Evolution Reaction. *J. King Saud Univ. Sci.* **2021**, *33* (3), 101379.

(23) Tran, Y. B. N.; Nguyen, P. T. K.; Luong, Q. T.; Nguyen, K. D. Series of M-MOF-184 (M = Mg, Co, Ni, Zn, Cu, Fe) Metal−Organic Frameworks for Catalysis Cycloaddition of CO_2. *Inorg. Chem.* **2020**, *59* (22), 16747−16759.

(24) Zhang, M.; Hu, D.; Xu, Z.; Liu, B.; Boubeche, M.; Chen, Z.; Wang, Y.; Luo, H.; Yan, K. Facile Synthesis of Ni-, Co-, Cu-Metal Organic Frameworks Electrocatalyst Boosting for Hydrogen Evolution Reaction. *J. Mater. Sci. Technol.* **2021**, *72*, 172−179.

(25) Xin, J.; Pang, H.; Gómez-García, C. J.; Jin, Z.; Wang, Y.; Au, C.-M.; Ma, H.; Wang, X.; Yang, G.; Yu, W.-Y. Nitrogen Doped 1 T/2H Mixed Phase MoS2/CuS Heterostructure Nanosheets for Enhanced Peroxidase Activity. *J. Colloid Interface Sci.* **2024**, *659*, 312−319.

(26) Fu, S.; Ullah Khan, S.; Yang, R.; Pang, H.; Au, C.-M.; Ma, H.; Wang, X.; Yang, G.; Sun, W.; Yu, W.-Y. High-Performance Heterometallic Photocatalysts Afforded by Polyoxometalate Synthons for Efficient H2 Production. *J. Colloid Interface Sci.* **2024**, *666*, 496−504.

(27) Du, X.; Xu, G.; Zhu, C.; Zhou, T.; Shi, P.; Gao, G. Copper/Cobalt Metal-Organic Framework Composites for Advanced Anode Material of Lithium-Ion Battery. *J. Energy Storage* **2024**, *89*, 111863.

(28) Mehek, R.; Iqbal, N.; Noor, T.; AmjadAli, M. Z. G.; Vignarooban, K.; Khan, M. A.; Khan, M. A. Metal−Organic Framework Based Electrode Materials for Lithium-Ion Batteries: A Review. *RSC Adv.* **2021**, *11* (47), 29247−29266.

(29) Zhao, R.; Liang, Z.; Zou, R.; Xu, Q. Metal-Organic Frameworks for Batteries. *Joule* **2018**, *2* (11), 2235−2259.

(30) Zhang, W.; Guo, X.; Wang, Y.; Zheng, Y.; Zhao, J.; Xie, H.; Zhang, Z.; Zhao, Y. Self-Assembly of Ni-Doped Co-MOF Spherical Shell Electrode for a High-Performance Supercapacitor. *Energy Fuels* **2022**, *36* (3), 1716−1725.

(31) Ensafi, A. A.; Fazel, R.; Rezaei, B.; Hu, J.-S. Copper-Nickel Rubeanate Metal-Organic Framework, a New Highly Stable and Long Active Life Nanocomposite for High-Performance Supercapacitors. *J. Materiomics* **2022**, *8* (4), 843−851.

(32) Zhao, S.; Zeng, L.; Cheng, G.; Yu, L.; Zeng, H. Ni/Co-Based Metal-Organic Frameworks as Electrode Material for High Performance Supercapacitors. *Chin. Chem. Lett.* **2019**, *30* (3), 605−609.

(33) Ali, A.; Waris; Basree; Khan, M. Z.; Dege, N.; Ahmad, M.; Shahid, M. Bifunctional Cu(ii)-Based 2D Coordination Polymer and Its Composite for High-Performance Photocatalysis and Electrochemical Energy Storage. *Dalton Trans.* **2023**, *52* (42), 15562−15575.

(34) Basree; Waris; Ali, A.; Khan, N.; Khan, M. Z.; Nayak, G. C.; Siddiqui, K. A.; Ahmad, M. A Dual Functional Cu(ii)-Coordination Polymer and Its RGO Composite for Selective Solvent Detection and High Performance Energy Storage. *Mater. Adv.* **2024**, *5* (20), 8265−8279.

(35) Basree; Ali, A.; Kumari, K.; Ahmad, M.; Nayak, G. C. Functional Metal−Organic Frameworks Derived Electrode Materials for Electrochemical Energy Storage: A Review. *Chem. Commun.* **2024**, *60*, 13292.

(36) Maranescu, B.; Visa, A. Applications of Metal-Organic Frameworks as Drug Delivery Systems. *Int. J. Mol. Sci.* **2022**, *23* (8), 4458.

(37) Gautam, S.; Lakhanpal, I.; Sonowal, L.; Goyal, N. Recent Advances in Targeted Drug Delivery Using Metal-Organic Frameworks: Toxicity and Release Kinetics. *Next Nanotechnol.* **2023**, 3−4, 100027.

(38) Lawson, H. D.; Walton, S. P.; Chan, C. Metal−Organic Frameworks for Drug Delivery: A Design Perspective. *ACS Appl. Mater. Interfaces* **2021**, *13* (6), 7004−7020.

(39) Ismail, R. M. A.; Enemose, E. A.; Al-Jamal, M.; Ramachandran, S. K.; Al-Mattarneh, H.; Gangodkar, D. Co-MoF Derived Colorimetric Sensors for Detection of Environmental Toxic Heavy Metal Analysis. *Adv. Sci. Technol.* **2022**, *117*, 43−49.

(40) Yuniasari, R.; Amri, F.; Abrori, S. A.; Septiani, N. L. W.; Rezki, M.; Irzaman; Fahmi, M. Z.; Yuliarto, B. A Graphene-Modified Co-BDC Metal-Organic Frameworks (Co-MOF) for Electrochemical Non-Enzymatic Glucose Sensing. *IOP Conf. Ser. Mater. Sci. Eng.* **2021**, *1045* (1), 012010.

(41) Nguyen, D.-K.; Lee, J.-H.; Doan, T. L.-H.; Nguyen, T.-B.; Park, S.; Kim, S. S.; Phan, B. T. H2 Gas Sensing of Co-Incorporated Metal-Organic Frameworks. *Appl. Surf. Sci.* **2020**, *523*, 146487.

(42) Mínguez Espallargas, G.; Coronado, E. Magnetic Functionalities in MOFs: From the Framework to the Pore. *Chem. Soc. Rev.* **2018**, *47* (2), 533−557.

(43) Zhang, Q.; Li, B.; Chen, L. First-Principles Study of Microporous Magnets M-MOF-74 (M = Ni, Co, Fe, Mn): The Role of Metal Centers. *Inorg. Chem.* **2013**, *52* (16), 9356−9362.

(44) Jiang, Z.; Gao, L.; Zhang, Y.; Hu, T. Synthesis Structure and Magnetic Properties of Two Isostructural Co/Mn (II) Metal Organic Frameworks. *Inorg. Chem. Commun.* **2022**, *141*, 109534.

(45) Yang, X.; Xu, Q. Bimetallic Metal−Organic Frameworks for Gas Storage and Separation. *Cryst. Growth Des.* **2017**, *17* (4), 1450−1455.

(46) Evans, A.; Cummings, M.; Decarolis, D.; Gianolio, D.; Shahid, S.; Law, G.; Attfield, M.; Law, D.; Petit, C. Optimisation of Cu $^+$ Impregnation of MOF-74 to Improve CO/N $_2$ and CO/CO $_2$ Separations. *RSC Adv.* **2020**, *10* (9), 5152−5162.

(47) Montoro, C.; Kim, J.-Y.; Mirzaei, A.; Lee, J.-H.; Sayegh, S.; Makhoul, E.; Iatsunskyi, I.; Coy, E.; Bechelany, M.; Kim, H. W.; Kim, S. S. MOF-Derived Metal Oxide (Cu, Ni, Zn) Gas Sensors with Excellent Selectivity towards H2S, CO and H2 Gases. *Composites, Part B* **2024**, *283*, 111637.

(48) Perera, A. A. P. R.; Madhushani, K. A. U.; Kumar, A.; Gupta, R. K. Metal-Organic Frameworks for Wastewater Treatment: Recent Developments, Challenges, and Future Prospects. *Chemosphere* **2023**, *339*, 139713.

(49) Kaur, H.; Devi, N.; Siwal, S. S.; Alsanie, W. F.; Thakur, M. K.; Thakur, V. K. Metal−Organic Framework-Based Materials for Wastewater Treatment: Superior Adsorbent Materials for the Removal of Hazardous Pollutants. *ACS Omega* **2023**, *8* (10), 9004−9030.

(50) Goswami, A.; Ghosh, D.; Chernyshev, V. V.; Dey, A.; Pradhan, D.; Biradha, K. 2D MOFs with Ni(II), Cu(II), and Co(II) as Efficient Oxygen Evolution Electrocatalysts: Rationalization of Catalytic Performance *vs* Structure of the MOFs and Potential of the Redox Couples. *ACS Appl. Mater. Interfaces* **2020**, *12* (30), 33679−33689.

(51) Somnath; Waris; Ali, A.; Ahmad, M.; Siddiqui, K. A. Bifunctional Self-Penetrating Co(II)-Based 3D MOF for High-Performance Environmental and Energy Storage Applications. *Cryst. Growth Des.* **2022**, *22* (12), 7374−7394.

(52) Liu, Q.; Guo, Z.; Wang, C.; Guo, S.; Xu, Z.; Hu, C.; Liu, Y.; Wang, Y.; He, J.; Wong, W. A Cobalt-Based Metal-Organic Framework Nanosheet as the Electrode for High-Performance Asymmetric Supercapacitor. *Advanced Science* **2023**, *10* (18), 2207545.

(53) Dolomanov, O. V.; Bourhis, L. J.; Gildea, R. J.; Howard, J. A. K.; Puschmann, H. *OLEX2*: A Complete Structure Solution, Refinement and Analysis Program. *J. Appl. Crystallogr.* **2009**, *42* (2), 339−341.

(54) Bourhis, L. J.; Dolomanov, O. V.; Gildea, R. J.; Howard, J. A. K.; Puschmann, H. The Anatomy of a Comprehensive Constrained, Restrained Refinement Program for the Modern Computing Environment − *Olex2* Dissected. *Acta Crystallogr., Sect. A:Found. Adv.* **2015**, *71* (1), 59−75.

(55) Shevchenko, A. P.; Blatov, V. A. Simplify to Understand: How to Elucidate Crystal Structures? *Struct. Chem.* **2021**, *32* (2), 507−519.

(56) Blatov, V. A.; Shevchenko, A. P.; Proserpio, D. M. Applied Topological Analysis of Crystal Structures with the Program Package ToposPro. *Cryst. Growth Des.* **2014**, *14* (7), 3576−3586.

(57) Bhoite, A. A.; Hubale, V. B.; Sawant, V. A.; Tarwal, N. L. Cobalt-Based Metal−Organic Framework (Co-MOF) Thin Films with High Capacitance for Supercapacitor Electrode. *J. Mater. Sci.* **2024**, *59* (16), 6807−6819.

(58) Ntoukas, I.; Lan, R.; Milanese, C.; Walker, M.; Donne, S. W.; Roberts, A. J.; Gkanas, E. I. Ni/Co Bimetallic Flower-like Metal−Organic Frameworks with Enhanced Performance for High-Power Energy Storage Applications. *MRS Commun.* **2024**, *14* (1), 69−75.

(59) Ghosh, S.; Maity, C. K.; Nayak, G. C.; Nayek, H. P. A Cobalt(II) Metal-Organic Framework Featuring Supercapacitor Application. *J. Solid State Chem.* **2020**, *282*, 121093.

(60) Deka, R.; Rathi, S.; Mobin, S. M. Exploring the Feasibility of a Two-Dimensional Layered Cobalt-Based Coordination Polymer for Supercapacitor Applications: Effect of Electrolytic Cations. *Energy Adv.* **2023**, *2* (12), 2119−2128.

(61) Sharma, P.; Ahmad, M.; Somnath; Haq, N.; Siddiqui, K. A. C−H···I Assisted 2D Cd(II)-Coordination Polymer: Remarkable Photocatalytic Degradation of Rose Bengal Dye and Efficient Colorimetric Recognition of La3+, and ClO4-. *J. Mol. Struct.* **2025**, *1319*, 139576.

(62) Zeng, X.; Zhang, Y.; Zhang, J.; Hu, H.; Wu, X.; Long, Z.; Hou, X. Facile Colorimetric Sensing of Pb 2+ Using Bimetallic Lanthanide Metal-Organic Frameworks as Luminescent Probe for Field Screen Analysis of Lead-Polluted Environmental Water. *Microchem. J.* **2017**, *134*, 140−145.

(63) Shukla, V.; Ahmad, M.; Nayak, G. C.; Thakur, T. S.; Siddiqui, K. A. High Cell Volume Zn-Metal−Organic Framework: Unveiling the Pseudo-Capacitor Properties and Selective Colorimetric Recognition of Oxyanions. *Cryst. Growth Des.* **2024**, *24* (9), 3977−3992.

(64) Gong, W.-J.; Yao, R.; Li, H.-X.; Ren, Z.-G.; Zhang, J.-G.; Lang, J.-P. Luminescent cadmium(ii) coordination polymers of 1,2,4,5-tetrakis(4-pyridylvinyl)benzene used as efficient multi-responsive sensors for toxic metal ions in water. *Dalton Trans.* **2017**, *46* (48), 16861−16871.

(65) Chen, J.; Yi, F.-Y.; Yu, H.; Jiao, S.; Pang, G.; Sun, Z.-M. Fast Response and Highly Selective Sensing of Amine Vapors Using a Luminescent Coordination Polymer. *Chem. Commun.* **2014**, *50* (72), 10506−10509.

(66) Shukla, V.; Ahmad, M.; Siddiqui, K. A. Colorimetric Recognition of a Biomarker of Trichloroethylene in Human Urine and Photocatalytic Dye Degradation Employing Unprecedented Co(II) MOF Luminescent Probe. *J. Mol. Struct.* **2024**, *1308*, 138068.